HAL
open science

Characterization of untransformed ferrite in 10Cr and 12Cr ODS steels

Anthony Durand, Denis Sornin, Yann De Carlan, Gabriel Spartacus, François Brisset, Ludovic Delbes, Benoît Baptiste, Thierry Baudin, Roland Logé

To cite this version:

Anthony Durand, Denis Sornin, Yann De Carlan, Gabriel Spartacus, François Brisset, et al.. Characterization of untransformed ferrite in 10Cr and 12Cr ODS steels. Materialia, 2021, 16, pp.101066. 10.1016/j.mtla.2021.101066 . hal-03287096v3

HAL Id: hal-03287096

https://hal.science/hal-03287096v3

Submitted on 13 Aug 2021

HAL is a multi-disciplinary open access archive for the deposit and dissemination of scientific research documents, whether they are published or not. The documents may come from teaching and research institutions in France or abroad, or from public or private research centers.

L'archive ouverte pluridisciplinaire **HAL**, est destinée au dépôt et à la diffusion de documents scientifiques de niveau recherche, publiés ou non, émanant des établissements d'enseignement et de recherche français ou étrangers, des laboratoires publics ou privés.

Characterization of untransformed ferrite in 10Cr and 12Cr ODS steels

Anthony DURAND[a*], Denis SORNIN[a], Yann de CARLAN[a], Gabriel SPARTACUS[a], François BRISSET[b], Ludovic DELBES[c], Benoît BAPTISTE[c], Thierry BAUDIN[b], Roland LOGÉ[d],

[a] Université Paris-Saclay, CEA, Service de Recherches Métallurgiques Appliquées, 91191, Gif-sur-Yvette, France.

[b] Université Paris-Saclay, CNRS, Institut de chimie moléculaire et des matériaux d'Orsay, 91405, Orsay, France.

[c] Sorbonne Université, UMR CNRS 7590, Institut de Minéralogie, de Physique des Matériaux et de Cosmochimie, 75005, Paris, France.

[d] EPFL, Material institute, LMTM. MCA1 258 (Bât. Microcity), rue de la Maladiére 71b-CP526, CH-2002 Neuchâtel, Switzerland.

* Corresponding author: anthony.durand2@cea.fr

Abstract:

Two new ferrito-martensitic oxide dispersion strengthened (ODS) steels reinforced with (Y, Ti, O) nanoparticles were elaborated using a high-energy attritor. The milled powder was consolidated by hot extrusion at 1050°C. The two types of ODS steels differ by chromium content, with 10 wt% Cr and 12 wt% Cr respectively. According to thermodynamic calculations, those grades are supposed to exhibit an austenitic transformation at high temperatures. X-ray diffraction (XRD) above austenitic temperature transformation reveals the presence of both ferrite and austenite phase. This unexpected ferrite phase is assumed to be untransformed low temperature ferrite. The α→γ phase transformation specific enthalpy is monitored by differential scanning calorimetry (DSC).The untransformed ferrite fraction is calculated using dilatometric data and confirmed by electron backscatter diffraction (EBSD) microstructural analysis. The quenched samples from the austenitic domain give an image of the high-temperature partitioning. EBSD maps reveal two distinct elementary microstructures, one martensitic inherited from austenite and the other corresponds to the untransformed ferrite. This untransformed ferrite keeps the crystallographic α-fiber conferred by hot-extrusion. The 10Cr ODS has equiaxed untransformed ferrite areas. In contrast, the untransformed ferrite into 12Cr ODS is distributed as elongated areas, parallel to the hot-extrusion direction. Moreover, electron probe micro analyzer (EPMA) mapping exhibits chromium content gradients, consistent with phase partitioning at high temperatures. Creep properties are evaluated at 650°C for both grades. Small-angle X-rays scattering (SAXS) shows a similar size and distribution of the oxide particles in both grades.

Keywords: ODS steel, untransformed ferrite, ferrito-martensitic steels, microstructure, SAXS, creep.

1. Introduction

Oxide dispersion strengthened (ODS) steels have been developed, for nuclear applications, to improve the very high-temperature properties of body-centered stainless steel. The addition of very fine stable particles at high temperatures is a promising solution [1,2]. ODS steels were considered as a potential structural and cladding material for GEN IV sodium-cooled fast reactors (SFR) [3,4], and fusion reactors [5]. Not only ODS steels exhibit a convenient void swelling resistance under irradiation but also they display interesting high-temperature mechanical properties [6]. Indeed, body-centered cubic lattice, like ferrito-martensitic matrix, exhibit very good intrinsic resistance to swelling compared to face-centered cubic lattice. If ferritic ODS steels are a good candidate for SFR development [7], manufacturing remains challenging. Manufacturing thin cladding tubes requires cold forming operations. Material recovery between rolling passes is necessary, at least to soften the materials and control the grain morphology [8]. Regarding this problem, a ferrito-martensitic grade exhibits the great advantage of a phase transformation at high temperatures which is efficient to recover microstructures [9,10]. Nevertheless, regarding fuel reprocessing envisaged in the SFR framework, low chromium grades are not the most relevant because of their excessive corrosion

during fuel acid dissolution. Thus, with a phase transformation at a sufficiently high temperature, 10Cr to 12Cr ODS steels are promising candidates offering easier manufacturing steps and interesting creep properties. Recent studies have evidenced improved creep properties of ODS steel attributed to untransformed ferrite above the ferrite to austenite phase transformation (α→γ) [11–13]. This enhancement is attributed to the nano-sized oxides which are smaller in ferrite than in martensite [14]. Particularly, such ODS steels containing untransformed ferrite are known to contain a double dispersion with smaller nano-sized oxides into the untransformed ferrite and bigger into the martensite matrix [11,12]. In that view, the chemical composition of the 12Cr steel of this study was adapted trying to retain some untransformed ferrite at high temperatures.

This study highlights the untransformed ferrite existence. For two different ODS steels, varying chromium content, a methodology based on dilatometric data and microstructural observations is proposed to quantify the untransformed ferrite fraction. Creep properties and nano-sized oxides dispersion are compared for the two materials.

2. Materials and methods

Both ODS steels, of this study, have a very close chemical composition. The first one is 10 wt% chromium and the second one is 12 wt%. The pre-alloyed powder was mechanically alloyed in a high-energy attritor with 0.1 wt% of TiH_2 powder and 0.3 wt% of Y_2O_3 powder under a helium atmosphere. The milled powder was sealed into a 64 mm diameter can and outgassed. Then, the powder was consolidated into a rod by hot-extrusion at 1050°C. The final product is a 23 mm diameter rod, the extrusion ratio is 9.8. Table 1 shows the chemical composition of the bulk materials after hot-extrusion. The manufacturing route is the same for both materials 10Cr ODS and 12Cr ODS.

	10Cr ODS (wt%) (Ref. CEA P42)	**12Cr ODS (wt%)** (Ref. CEA P43)
Cr	9.7	11.5
W	0.88	0.87
Mn	0.26	0.26
Mo	0.45	0.44
Ni	0.31	0.3
Ti	0.22	0.25
C	0.11	0.12
O	0.12	0.1
Al	0.01	0.01
Si	0.06	0.07
N	0.004	0.009
Y	0.21	0.21

Table 1 : Chemical composition of the bulk produced materials. Ti and Y are measured by plasma emission spectrometry. C, O and N are respectively measured by combustion infrared absorption, reducing melting infrared absorption and reducing melting thermal conductivity. The other elements are measured by optical emission spectroscopy.

The X-ray diffraction (XRD) at low and high temperatures was conducted on Panalytical Xper't Pro MPD equipment coupled to a controlled-atmosphere furnace from Anton Paar HTK. The X-ray source is a cobalt source with a wavelength of 1.79 Å. To avoid excessive sample oxidation the heating chamber is maintained under vacuum (10^{-3} mBar).

Dilatometric experiments were conducted on a DT1000 ADAMEL-LHOMARGY dilatometer on 12x2x2 mm^3 samples picked-up in the longitudinal direction of the rod.

Differential scanning calorimetry (DSC), using a SETARAM MHTC96 equipment, measures phase transformation specific enthalpy.

Scanning electron microscopy using the electron backscatter diffraction (EBSD) detector were performed on gas-quenched samples, heat-treated into the dilatometer. EBSD maps analysis were completed with quantitative electron probe micro analyzer (EPMA) mapping using Cameca SX100 equipment.

Creep properties were evaluated at 650°C, under air atmosphere, on cylindrical samples of 4 mm diameter and 20 mm gauge length. Samples were machined with the tensile direction collinear to the hot-extrusion flow. Materials tested were heat-treated at 1050°C for one hour, completed by a furnace cooling (2°C/min).

ODS steels are well known to exhibit a nano-sized oxides dispersion [15], whose size and density were evaluated by small angle X-ray scattering (SAXS) measurements in transmission mode. In this study, the samples thickness is grinded down to $25\ \mu m$ in order to achieve a suitable transmission regarding the energy used. Experiments were performed at the cSAXS beamline, Swiss light source (SLS), at the Paul Scherrer Institute (PSI). The energy of the X-ray beam is $4.766\ keV$ with a detector to sample distance around 2 m. Scattering patterns were acquired on two distinct 2D detectors in order to cover a wider scattering vector q-range. Acquisition time was set to 10 seconds and 15 frames were measured and averaged for each specimen. The two scattering patterns coming from the two detectors were both azimuthally integrated, background-corrected, normalized by incident intensity, sample thickness, transmission and their respective solid angle. Both intensities were then reduced to absolute units thanks to a secondary glassy carbon standard.

The interaction between the X-ray beam and the sample produces the scattered signal, which is collected by the detector. The signal obtained is intensity as a function of the scattering vector q,

$$|\vec{q}| = \frac{4\pi}{\lambda}\sin(\theta) \qquad (1)$$

where λ is the wavelength of the applied radiation and 2θ the scattering angle.

The intensity profile is linked to several characteristics of the scattering object [16]. The scattering of N dispersed particles and correctly diluted into a matrix is:

$$\Delta I(q) = I_0 * \sum_{i=1}^{N} V_i^2 * (\Delta\rho)_i{}^2 * P_i(q) \qquad (2)$$

where I_0 is the incident beam intensity, V_i the volume of the particle i, P the form factor of precipitates assumed as spherical. $\Delta\rho$ the electronic contrast (difference in scattering length) between the particles and the matrix and depends on the X-ray beam wavelength (λ). The scattering length density is also dependent on the chemical composition and the mean atomic volume according to the equation (3). Then precipitates are assumed mainly $Y_2Ti_2O_7$ pyrochlores. In order to determine the value of $\Delta\rho$, knowing that the matrix is a ferritic Fe-10/12Cr-1W system, scattering length density was determined thanks to tabulated data from Henke et al. study [17].

$$\rho = \sum_{\substack{chemical\\elements}} \frac{x_i}{V_{molecular}} * b_i(\lambda) \qquad (3)$$

Where $b_i(\lambda)$ is the scattering cross-section of the element i, proportional to the atomic scattering factor.

Finally, the scattering length density values for 10Cr ODS and 12Cr ODS are $5.95\ .10^{-5}\ \text{Å}^{-2}$ and $5.93\ .10^{-5}\ \text{Å}^{-2}$ respectively. For the $Y_2Ti_2O_7$ particles, the value is $3.18\ .10^{-5}\ \text{Å}^{-2}$. Those equations are employed to fit the experimental values using a Monte Carlo algorithm. McSAS software is used to perform this fit [18,19]. The output data are the radius number distribution and the radius volume fraction distribution of the scattered particles. From those outputs, the mean radius and the number density of precipitates are estimated.

3. Results and discussion

3.1. Untransformed ferrite highlight

The Fe-Cr binary diagram presented in Figure 1 is computed based on ThermoCalc software using TCFE5 database. This diagram is based on the chemical composition, identified in Table 1. The minor elements (Al, Si and N) are not taken into account. Yttrium is also not used in the chemical composition, supposed to be contained only in nano-sized oxides. Thus, the presented diagram is equivalent to the materials of the study without the oxide dispersion contribution. This diagram shows, at 1050°C, a fully austenitic material for 10Cr ODS. The 12Cr ODS is also fully austenitic but very close to the dual-phase domain.

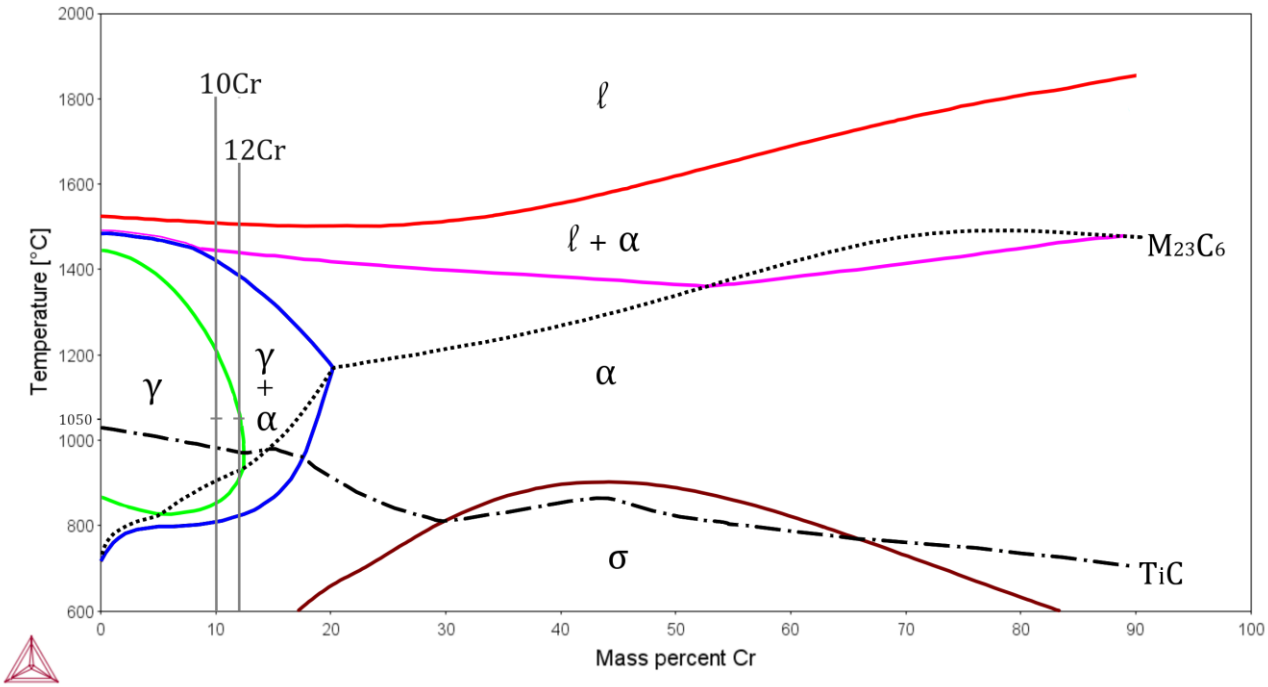

Figure 1: Calculated Fe-Cr binary diagram corresponding to the chemical composition of the experimental materials.

Dilatometric tests were conducted to identify experimentally the α→γ transformation temperatures. The thermal expansion was measured in hot-extrusion direction (ED). The heating rate was set to 1°C/s from room temperature to 1100°C to approach the equilibrium transformation avoiding an excessive dwell time that could influence the sample microstructure (decarburization). Before cooling, the samples were kept at 1100°C for two minutes. The α→γ temperatures transformation during heating are presented in Table 2. These temperatures are close to ODS steels data from the literature [20]. The shift to higher temperatures compared to steels without oxide dispersion is also in agreement with the observations on 9 wt% Cr ODS steel [8,10] and ODS EUROFER [21]. The temperatures of the beginning and the end of the transformation are shifted up by about 20°C for the 12Cr ODS compared to the 10Cr ODS. This is consistent with the shape of the Fe-Cr binary diagram, which illustrates such a shifting with Cr content.

	10Cr ODS	**12Cr ODS**
Ac_1 (°C)	941.7 (5.1)	963.0 (2.1)
Ac_3 (°C)	981.7 (7.1)	998.1 (2.7)

Table 2: Temperature of the α→γ transformation for a 1°C/s heating rate with standard deviation in the brackets.

To detect the presence of ferrite into the austenitic matrix upon the transformation temperature Ac_3, XRD measurements are done.

The two materials are prepared with the same protocol to highlight the contribution of chromium content. Samples were prepared from a bulk part heat-treated at 1050°C for one hour followed by slow cooling ensuring a ferritic state at the beginning of the XRD measurements. Four different measurements were conducted at various temperatures: the initial state at 25°C, the heated material at 1050°C, the heated materials at 1050°C twenty minutes after reaching shelf temperature and finally the ferritic cooled state back to 25°C. The prospected angle extent is [48°, 56°] including the (111) austenite and (110) ferrite diffraction peaks. The theoretical position of those two peaks is 50.2° and 52.2°, respectively, according to the Bragg law with a cobalt source. The XRD results of 10Cr ODS and 12Cr ODS are presented in Figure 2.

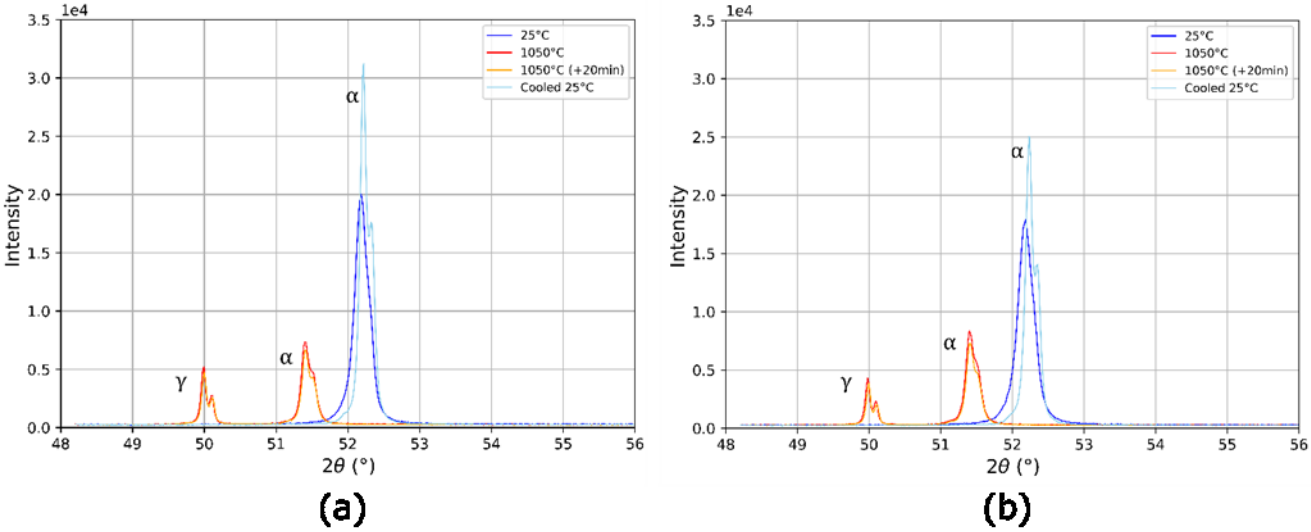

Figure 2: XRD at 25°C of the initial ferritic state, 1050°C and 25°C after a slow cooling for (a) 10Cr ODS and (b) 12Cr ODS.

At 25°C both materials are constituted of ferrite and only one peak at 2θ = 52.2° is noticed corresponding to the (110) ferritic peak. This peak is strongly enhanced by the crystallographic fiber inherited from hot-extrusion. At 1050°C, two peaks are noticed: one at 2θ = 50.0° for both materials and a second one at 2θ = 51.4°. According to Bragg's law, the first one is associated with the austenitic phase diffraction and the second one is a ferritic peak. This second peak offsets to lower angles compared to room temperature. This is a consequence of the thermal expansion of the sample. The two peaks evidence the coexistence of both ferrite and austenite above the α→γ transformation temperature. Moreover, twenty minutes after reaching 1050°C the ferrite is still present on XRD measurements. The ferritic phase seen at 1050°C is arguably the initial ferrite that does not undergo the phase transformation during the heating procedure.

To compare both materials, the quantification of the untransformed ferrite volume fraction is necessary. One way is to use dilatometric data. When considering the material above Ac_3, composed of a volume fraction (x) of untransformed ferrite and a volume fraction (1-x) of austenite, the thermal expansion coefficient of this material, is assumed to be a fraction combination of the coefficient of the two phases. Then, after austenitization at high temperatures, the thermal expansion coefficient is expressed as:

$$\alpha_{ODS} = x * \alpha_{ODS}^{F} + (1 - x) * \alpha_{ODS}^{A} \qquad (4)$$

Where α_{ODS} is the material thermal expansion coefficient of the characterized ODS steel, α_{ODS}^{F} is the thermal expansion coefficient of the ODS in the fully ferritic state and α_{ODS}^{A} is the thermal expansion coefficient of a fully austenitic state.

α_{ODS} is calculated with a temperature interval of 5°C during the heating (1°C/s) between 1000°C and 1100°C, the growth with the temperature is linear. Numerous measures are used, giving the standard deviation of α_{ODS}.

The materials follow an α→γ transformation around 950°C. To estimate α_{ODS}^{F}, the thermal expansion coefficient of the ODS material is calculated between 250 and 800°C (i.e., fully ferritic range) with a temperature interval of 5°C during heating at 1°C/s. The expansion evolution with the temperature is linearly between 250°C and 800°C, and then it is assumed that the value can be extrapolated between 1000°C and 1100°C. The calculated values for the ferritic state are in agreement with data issued from literature : $12 - 14\ .10^{-6}\ °C^{-1}$ [11,22].

Using dilatometric data from 9 wt% of chromium ODS steels [23] which is fully austenitic above Ac_3, α_{ODS}^{A} is evaluated. The obtained value is $19.70\ .10^{-6}\ °C^{-1}$ which is in agreement with other literature data [11,24].

	$\boldsymbol{\alpha_{ODS}^{F}}$ $(\mathbf{10^{-6}\ °C^{-1}})$	$\boldsymbol{\alpha_{ODS}}$ $(\mathbf{10^{-6}\ °C^{-1}})$
$10Cr$ ODS	12.36	16.67 (0.08)
$12Cr$ ODS	12.32	16.11 (0.27)

Table 3: Calculated thermal expansion coefficient of 10Cr ODS and 12Cr ODS in a fully ferritic state at low temperature and in the austenitic domain at high-temperature with standard deviation in the brackets.

Therefore, eq. 4 gives the volume fraction of untransformed ferrite, reported in Table 4.

	$\boldsymbol{untransformed\ ferrite}$ (%)
$10Cr$ ODS	41.2 ± 1.2
$12Cr$ ODS	48.8 ± 3.7

Table 4 : Volume fraction of untransformed ferrite in the 10Cr ODS and in the 12Cr ODS calculated from eq. 4 using dilatometric data.

Dilatometric data illustrate a volume fraction of untransformed ferrite significantly more important for 12Cr ODS compared to 10Cr ODS. To confirm this tendency, DSC measurements are performed during the α→γ transformation to compare the specific enthalpy of the phase transformation for 10Cr ODS and 12Cr ODS materials.

The DSC heating rate chosen is very low (10°C/min) to approximate thermodynamic equilibrium conditions. The sample is heated from 25°C to 1350°C. Samples stayed 5 min at 1350°C before cooling at a rate of 10°C/min. In those conditions, the signal gives access to the specific enthalpy of phase transformation during heating. Figure 3 shows the evolution of the heat flow as a function of the temperature for both materials.

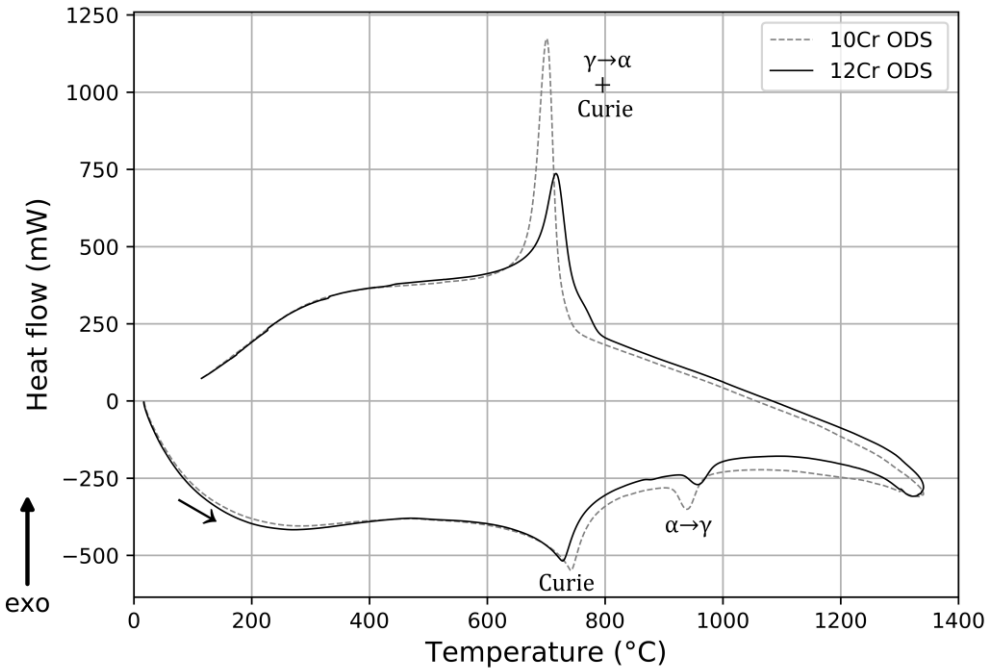

Figure 3: DSC curves for a heating and cooling rate of 10°C/min for 10Cr ODS and 12Cr ODS.

As presented in Figure 3 the behavior of both materials is similar during the heating sequence. The first peak, around 750°C, is the Curie peak, characteristic of ferrous alloys. The second peak, around the 950°C, represents the α→γ transformation. The characteristic temperatures of both materials are slightly different. This difference is due to the increase of the chromium content that shifts up those temperatures. The main advantage of DSC measurement is the quantification of the phase transformation specific enthalpy. To get this quantity the onset/offset method is used with a linear regression between the beginning and the end of the phase transformation. The area between the regression and the DSC peak is calculated. Thus, that integration gives the specific enthalpy of the phase transformation. The specific enthalpy values are presented in Table 5.

	$\Delta H\ (J/g)$
10Cr ODS	4.949
12Cr ODS	3.286

Table 5: Specific enthalpy of the α→γ transformation with a heating rate of 10°C/min for 10Cr ODS and 12Cr ODS.

The specific enthalpy is 1.5 higher for the 10Cr ODS than for the 12Cr ODS. This is in agreement with the dilatometric quantification of the untransformed ferrite. The higher specific enthalpy means that a higher volume of material changes phase. Additionally, the DSC measurements do not reveal the existence of δ-ferrite at 1350°C. There is no visible phase transformation above the ferrite to austenite transformation. The ferrite observed at 1050°C is untransformed ferrite during heating.

3.2. Microstructure

XRD measurements have revealed untransformed ferrite after austenitization heat treatment. EBSD maps give complementary information. They precise the spatial distribution of the untransformed ferrite. Microstructural observations are focused on a martensitic quenched state, which is an image at room temperature of the high-temperature microstructure. The Figure 4 shows the dilatation signals of the samples during heat treatment.

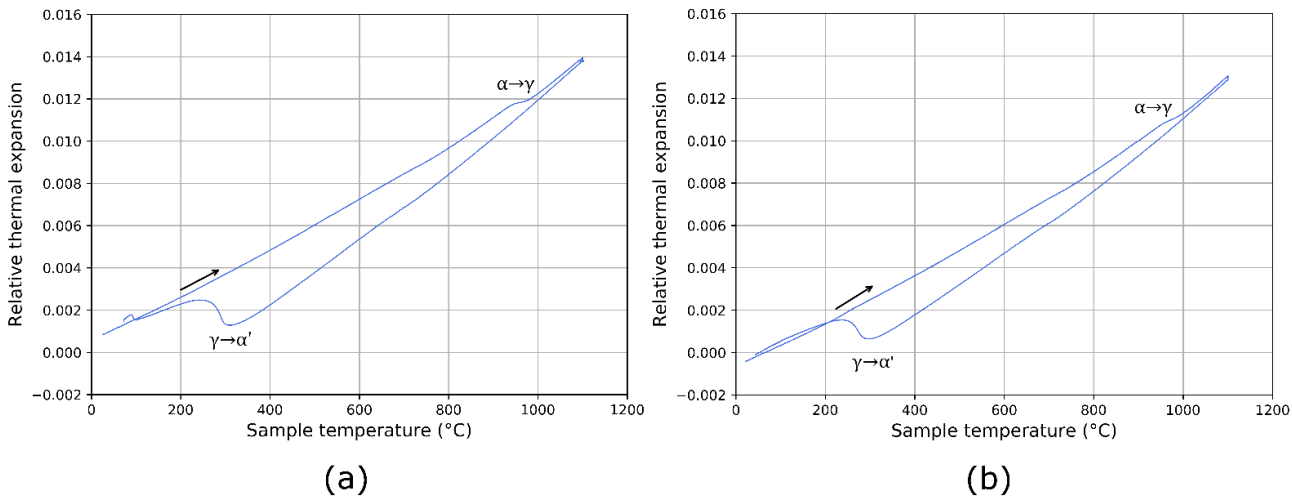

Figure 4: Thermal expansion measurements during heating at 1°C/s from 25°C to 1100°C following by quenching at 10°C/s until 25°C for (a) 10Cr ODS and (b) 12Cr ODS.

Figure 4 shows that the entire amount of austenite is transformed into martensite during cooling. In fact, dilatometric curves only highlight a martensitic transformation. Quench transforms the austenite into martensite whereas ferrite is assumed to be unchanged. Consequently, after quenching, the two materials present a dual-phase structure with untransformed ferrite and martensite.

Figure 5 presents a large view of this metallurgical state, the EBSD map size is 400 x 400 µm² with a step size of 200 nm. A focus is also presented, which is a 100 x 50 µm² map acquired with a step size of 50 nm.

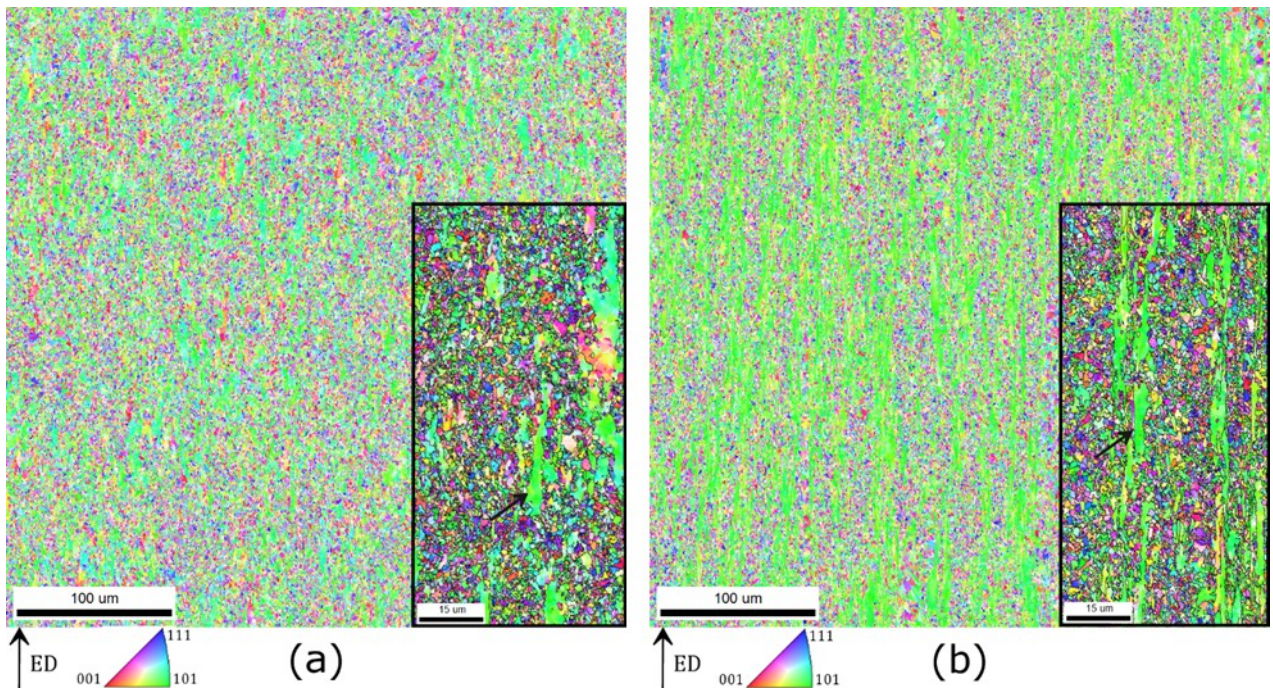

Figure 5: Inverse pole figure maps ⟨uvw⟩ direction parallel to the extrusion direction of the martensitic state of the (a) 10Cr ODS and (b) 12Cr ODS.

10Cr ODS and 12Cr ODS both present two different elementary microstructures. The first one, is constituted of elongated green grains corresponding to the fiber <110>//ED orientation (black arrows on Figure 5). The second is a cluster of grains with random orientation and an equiaxed shape. For 10Cr ODS, in the large view, there is an equiaxed distribution of these two elementary microstructures. On the contrary, the 12Cr ODS presents the two elementary microstructures distributed as elongated areas, like a columnar distribution. These elongated areas are parallel to

the hot-extrusion direction. Nonetheless, the focused map of the 10Cr ODS shows a few grains elongated and parallel with the hot-extrusion direction (pointed by black arrow).

Firstly, the α→γ transformation is supposed to confer a microstructure without privileged orientation to the materials. Thus, the domain exhibiting randomly orientated grains, is assumed to constitute the part of the material that changes phase. Secondly, the elementary microstructure with α-fiber grains is characteristic of a hot-extruded microstructure. The α-fiber is a main characteristic of hot-extruded material, especially for ferritic ODS steels [25]. Hence, the elongated green grains domains present a microstructure inherited from hot-extrusion, consistent with a lack of phase transformation [26]. These observations are strongly consistent with the untransformed ferrite evidence given by XRD measurements.

EBSD microstructures observations are in favour of the two phases coexistence at 1050°C. The solubility of chromium is different in ferrite and martensite. Besides, chromium is known to be a ferrite marker [27]. Then, a chromium partitioning can be consistent with the two phases coexistence at 1050°C. To access the local chemical composition, the martensitic state is studied using an electron probe micro analyzer (EPMA). The EPMA maps of martensitic state are presented in Figure 6. For the 12Cr ODS, the chromium content gradient is evidenced as long strips. A chromium content gradient is also seen in the 10Cr ODS. Unlike the 12Cr ODS, the distribution of the high and low chromium areas is equiaxed. The chromium content gradient into the 12Cr ODS is more important than the one of 10Cr ODS. The chromium content deviation between the nominal composition and the enriched areas is more important for 12Cr ODS (+ 2 wt%) than for 10Cr ODS (+ 1.5 wt%) as illustrated by the chromium profiles of Figure 7. For 12Cr ODS, enriched titanium areas are aligned with the hot-extrusion direction. The titanium map of 10Cr ODS shows poor titanium segregation.

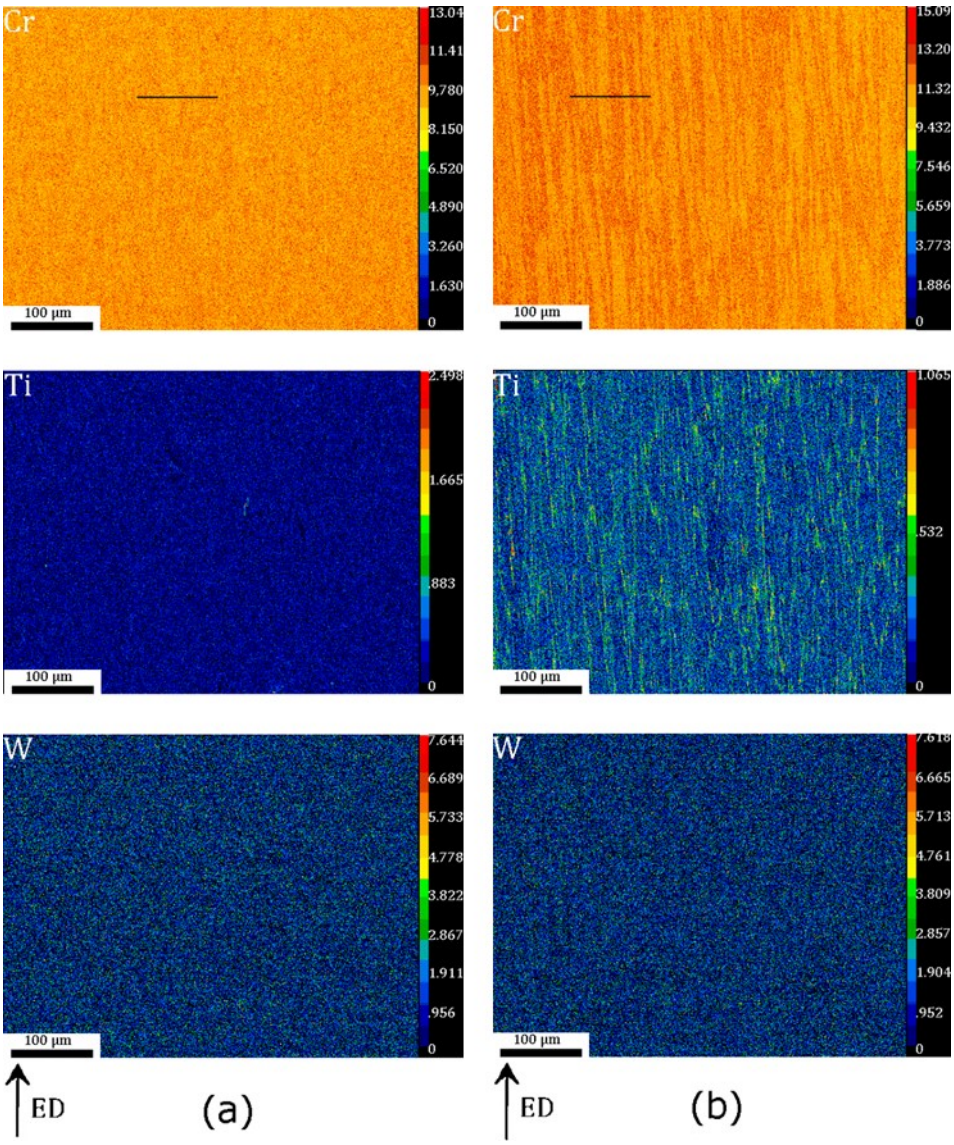

Figure 6: Quantitative EPMA mapping of the martensitic state of the (a) 10Cr ODS and (b) 12Cr ODS for Cr, Ti and W chemical elements.

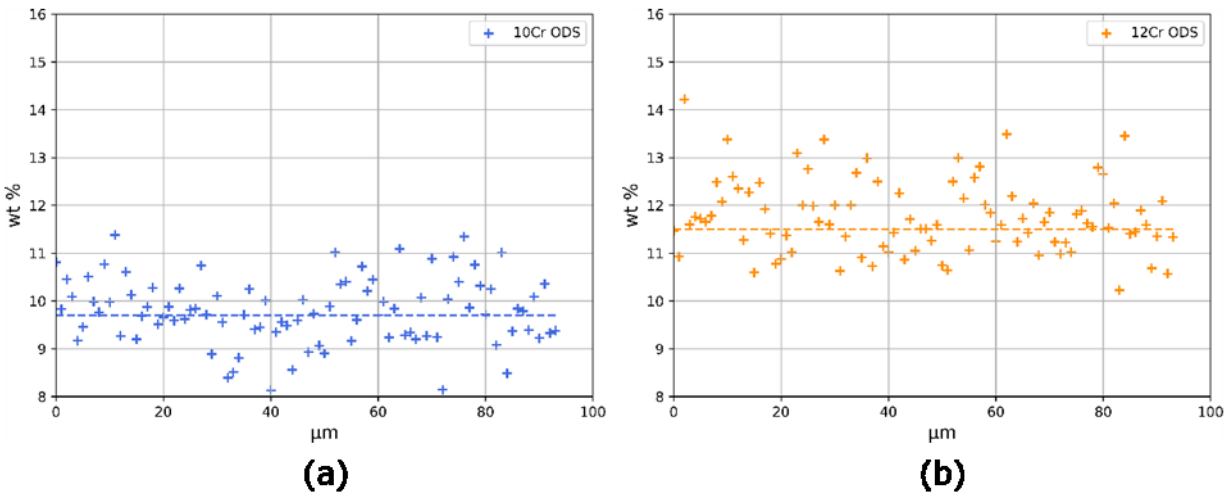

Figure 7: Chromium content evolution along lines marked on Figure 6-Cr of the (a) 10Cr ODS and (b) 12Cr ODS, the dotted line represents the measured mean composition from Table 1.

Chromium-enriched areas are composed of elongated grains, like elementary microstructures. This is in agreement with the EBSD observations of the untransformed ferrite. EPMA maps present a uniform distribution of tungsten, another ferrite stabilizer. Here the tungsten does not appears

segregated like chromium. This is not consistent with the work of Ohtsuka et al. [28]. Probably because the added tungsten amount is lower in the present study (1 wt% instead of 2 wt% for Ohtsuka et al. [28]) and the diffusion is too slow to induce a significant partitioning.

The EBSD observations are also used to estimate the untransformed ferrite fraction into the materials. The image quality (IQ) parameter from EBSD maps of the martensitic state is used to identify the two domains. IQ is the OIM software parameter to name the Kikuchi band contrast. The IQ value of the ferritic grains is greater than the one of the martensitic grains [29,30] due to lower geometrically necessary dislocations. To improve the contrast between the martensite and the untransformed ferrite, the average IQ per grain is preferred [31].

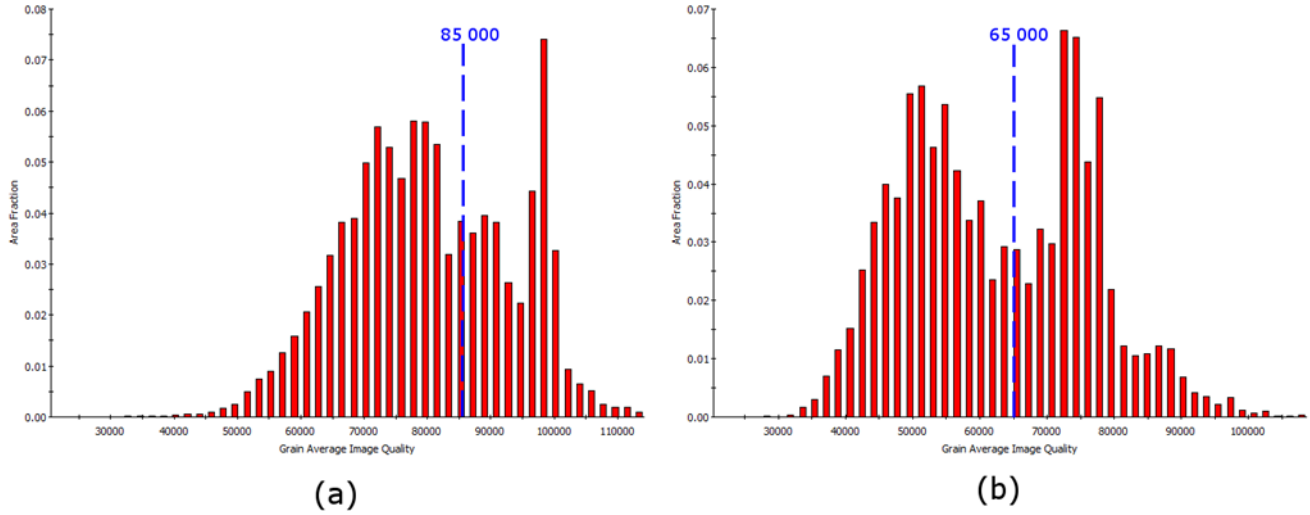

Figure 8: Average IQ distribution of the martensitic state of (a) 10Cr ODS and (b) 12Cr ODS.

The average IQ per grain is presented in Figure 8 for both materials. Two main domains of average IQ values are highlighted. The thresholds identified onto the diagram are applied to split the EBSD maps between martensite and ferrite as presented in Figure 9. Grains with an average IQ value under the threshold are plotted in red and assumed grains of martensite. The untransformed ferrite grains, plotted in blue, are assumed to be above the threshold.

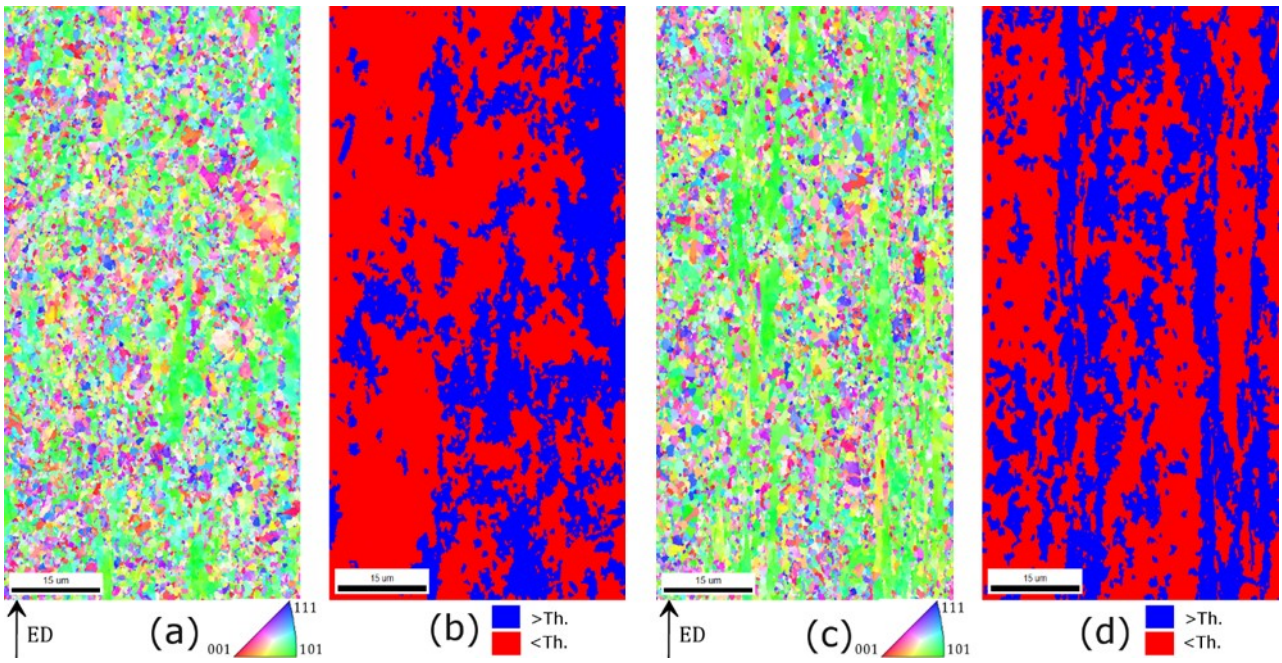

Figure 9: Inverse pole figure maps ‹uvw> direction parallel to the extrusion direction of (a) 10Cr ODS and (c) 12Cr ODS in martensitic state and IQ threshold map of (b) 10Cr ODS and (d) 12Cr ODS, martensite area are in red and untransformed ferrite area are in blue.

The blue areas, in Figure 9, match with the elementary microstructure of the α-fiber grains identified on the EBSD maps. Thus, the IQ threshold is in agreement with the crystallographic texture observations. This identification method offers the possibility to quantify the surface fraction of untransformed ferrite. Those surface fractions, reported in Table 6, are closed to the macroscopic dilatometric volume quantifications summarized in Table 4. The tendency is the same with less untransformed ferrite into the 10Cr ODS compared to the 12Cr ODS.

	$\boldsymbol{Untransformed\ ferrite}$ (%)
$10Cr$ ODS	36
$12Cr$ ODS	43

Table 6: Surface fraction of untransformed ferrite in 10Cr ODS and in 12Cr ODS using IQ threshold.

3.3. Creep properties

Table 7 presents the results of the thermal creep tests of the two materials. The tests are performed at 650°C under stresses of 210 MPa and 180 MPa.

	$\boldsymbol{\sigma}$ $(\boldsymbol{MPa})$	$\boldsymbol{T_r}$ $(\boldsymbol{h})$	$\boldsymbol{Creep\ rate}$ $(\boldsymbol{10^{-6}.h^{-1}})$	$\boldsymbol{Total\ strain}$ (%)
$10Cr$ ODS	210	206	26.3	5.02
	180	511	6.31	3.32
$12\ Cr$ ODS	210	286	42.4	4.61
	180	1275	2.75	2.74

Table 7: Thermal creep properties (Time to rupture, secondary creep rate and total strain) at 650°C of 10Cr ODS and 12Cr ODS for two different stress.

For the two considered loads, 10Cr ODS total stain is more important and the time to rupture (T_r) is lower than for 12Cr ODS. At the higher load, the creep rate of the 12Cr ODS is 1.5 times more important than for 10Cr ODS. This order is reversed for the lower load. The same observation was already reported by Muroga et al. [32].

Creep properties are usually split up into diffusive and dislocation creep contributions [33,34]. Diffusive creep is mainly dependent on the number of grain boundaries and then correlated to the grain size. To compare the contribution of the diffusive creep, the grain size of both materials is calculated using the intercept method and presented in Table 6. Because of an anisotropic microstructure, grain size is estimated in both longitudinal direction (collinear to the tensile direction) and in transverse direction. Vertically average intercept length is similar for both materials. Consequently, grain size cannot explain the differences observed in creep properties. Concerning the dislocation creep, the nano-sized oxide particles constitute barriers to the moving of the dislocations. A finer nano-sized oxides dispersion increase the dislocations pinning on the nano-sized oxides, decreasing the dislocation creep [20]. This effect is discussed in the section dedicated to oxide particle dispersion.

	Average intercept length (µm) (longitudinal)	**Average intercept length (µm) (transverse)**
$10Cr$ ODS	1.205	1.054
$12Cr$ ODS	1.100	0.948

Table 8: Grain size of the creep-tested microstructures using the intercept method, in the longitudinal direction and the transverse direction.

Figure 10 presents a Larson Miller graph taking into account several ODS steels from the literature. Materials of this study are compared to other ODS steel with 9 wt% of chromium [32,35,36] and 12 wt% of chromium but without Ni addition [32,35].

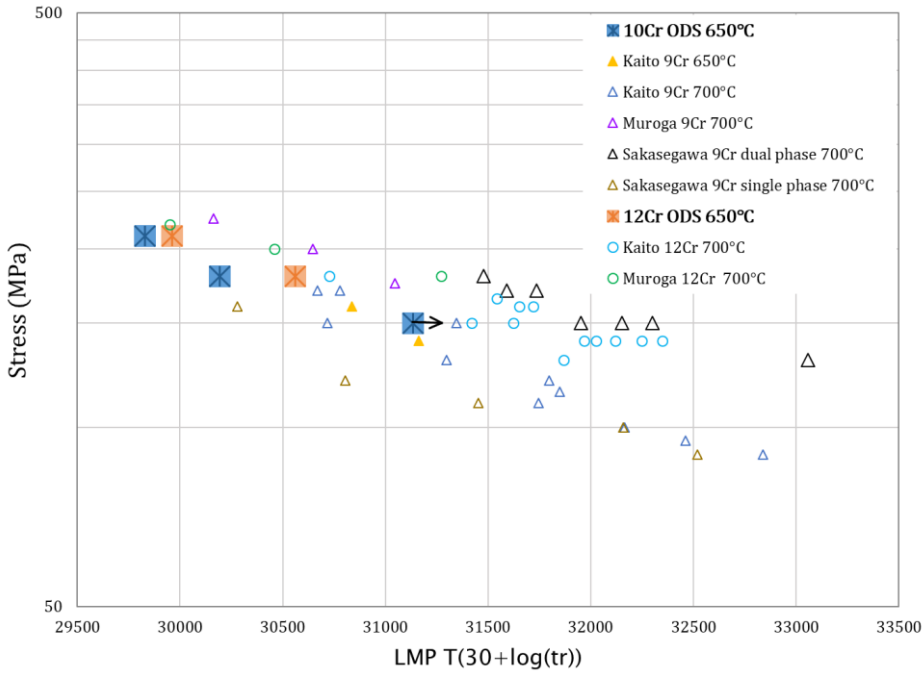

Figure 10: Larson Miller graph of the two ODS steel 10Cr ODS and 12Cr ODS compared with literature references. Arrow denotes ongoing test.

Both ODS steels of this study are close to the mean behavior of literature data prospected. The dual-phase 9Cr of Sakasegawa et al. [36] seems to present better properties. The authors attribute the main behavior difference between the dual and single-phase to the presence of residual ferrite. The 10Cr ODS of this study contains some untransformed ferrite and its creep behavior is between the 9Cr dual phase and the 9Cr single phase. This 9Cr dual-phase contains a volume fraction of about 25% of ferrite. This quantity is only half the amount of untransformed ferrite in 10Cr ODS or 12Cr ODS of the present study. A high volume fraction of untransformed ferrite is not a warranty of very high creep properties.

3.4. Oxide particles dispersion

The evaluation of the oxide particles size and number density is conducted for both materials using SAXS method. As referred to in the creep section, dislocation creep properties depend on the oxide particle sizes.

Figure 11 presents the scattering curves of both grades acquired in the same experimental conditions. The shape of the scattering curve looks very similar for the two materials. As illustrated by Figure 11, the linear asymptote observed at lower q is modified between $0.4\ nm^{-1}$ and $1.1\ nm^{-1}$ which is known to be the contribution of the nano-sized objects. Therefore, nano-sized oxides contributions are very similar for both materials.

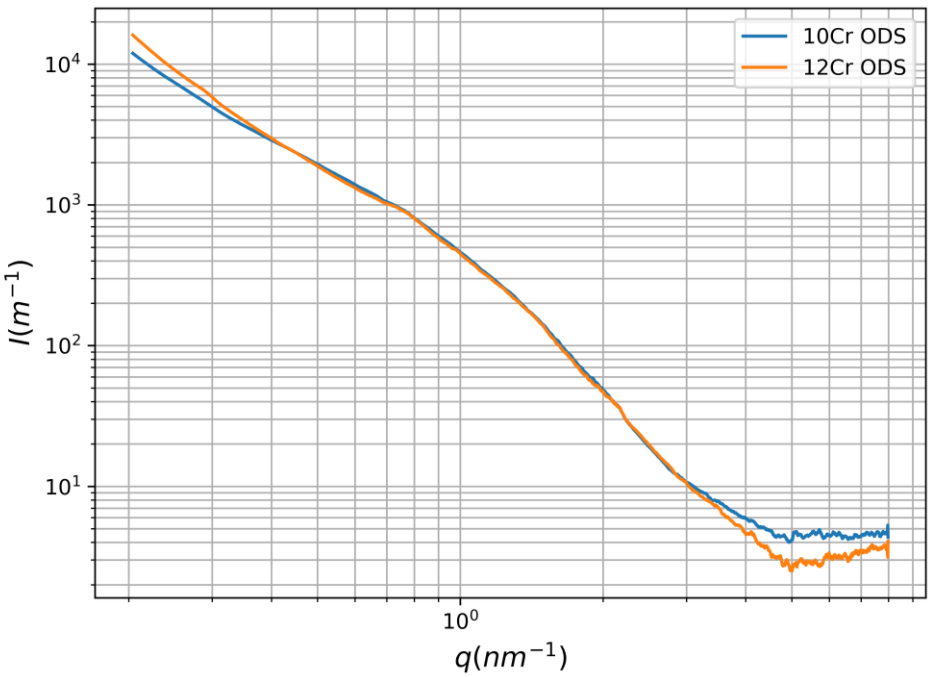

Figure 11: Scattering curve of the 10Cr ODS and 12 Cr ODS obtained at 4.766 keV.

Using the scattering data, Monte Carlo analyses are conducted. McSAS software is used to obtain the fit between the Monte Carlo analysis and the experimental data. The mean radius and the number density are calculated and referred to in Table 9.

	$r_{mean}(nm)$	$N\ (10^{23}\ m^{-3})$
10 Cr ODS	1.184	7.278
12 Cr ODS	1.179	7.271

Table 9: Mean radius obtained from the number distribution and number density of particles in 10Cr ODS and 12Cr ODS.

The mean radius and number density are very close to each other in both grades. Indeed, the two ODS grades follow the same manufacturing route. These values are in the range of common values referred to in the literature for such addition of Y_20_3 [15,37]. The SAXS measurements do not emphasize any double distribution of nano-sized oxides.

As mentioned in creep properties section, nano-sized oxides play a crucial role on dislocation creep. SAXS measurements disclose a similar size and density for both materials. Consequently, the effects of the nano-sized oxides on the dislocation creep is probably equivalent for the two materials. Only the distribution and fraction of untransformed ferrite are different in the microstructure of both materials.

4. Conclusions

The present study investigates the presence of untransformed ferrite at high temperatures into two ODS steels containing 10 wt% and 12 wt% of chromium respectively. These steels were elaborated with the same manufacturing route. XRD at 1050°C was used to evidence the existence of untransformed ferrite above the α→γ transformation temperature. This untransformed ferrite is still observed even after twenty minutes at 1050°C. The microstructure of both materials is studied using quenched samples to distinguish untransformed ferrite from martensite. The martensite corresponds to the fraction of materials that changes phase. Each grades is constituted of two different elementary microstructures. One of the two presents characteristics of a ferrite inherited from the hot-extrusion process. This elementary microstructure is superimposed with chromium-enriched areas, consistent with partitioning at high temperatures. The second elementary microstructure,

consistent with a martensitic structure, is assumed to be inherited from phase transformation. In addition, the IQ analysis of EBSD maps also reveals these two elementary microstructures. Both materials are tested in creep conditions. Results illustrate a slightly better behavior of the 12Cr ODS compared to 10Cr ODS. Regarding grain size and nano-size oxides dispersion, assumed to monitor diffusive and dislocation creep behavior respectively, these differences in creep properties cannot be explained. The only microstructural difference between both materials seems to be the distribution and fraction of untransformed ferrite.

Further creep investigations are necessary to confirm the effect of the untransformed ferrite on the mechanical properties.

Acknowledgements

We are thankful to Thomas Guilbert for dilatometric and DSC measurements. The authors are also grateful to Véronique Lezaud-Chaillioux and Florent Lefebvre for supporting the creep tests.

We acknowledge the Paul Scherrer Institut, Villigen, Switzerland for provision of synchrotron radiation beamtime at beamline cSAXS of the SLS and would like to thank Andreas Menzel for his assistance during the experiments.

References

[1] A. De Bremaecker, Past research and fabrication conducted at SCK•CEN on ferritic ODS alloys used as cladding for FBR's fuel pins, J. Nucl. Mater. 428 (2012) 13–30. https://doi.org/10.1016/j.jnucmat.2011.11.060.

[2] M.K. Miller, D.T. Hoelzer, E.A. Kenik, K.F. Russell, Stability of ferritic MA/ODS alloys at high temperatures, Intermetallics. 13 (2005) 387–392. https://doi.org/10.1016/j.intermet.2004.07.036.

[3] P. Dubuisson, Y. de Carlan, V. Garat, M. Blat, ODS Ferritic/martensitic alloys for Sodium Fast Reactor fuel pin cladding, J. Nucl. Mater. 428 (2012) 6–12. https://doi.org/10.1016/j.jnucmat.2011.10.037.

[4] S. Ukai, M. Fujiwara, Perspective of ODS alloys application in nuclear environments, J. Nucl. Mater. 307 (2002) 749–757.

[5] Z. Oksiuta, P. Olier, Y. de Carlan, N. Baluc, Development and characterisation of a new ODS ferritic steel for fusion reactor application, J. Nucl. Mater. 393 (2009) 114–119. https://doi.org/10.1016/j.jnucmat.2009.05.013.

[6] J.-J. Huet, L. Coheur, A.D. Bremaecker, L.D. Wilde, J. Gedopt, W. Hendrix, W. Vandermeulen, Fabrication and Mechanical Properties of Oxide Dispersion Strengthening Ferritic Alloy Canning Tubes for Fast Reactor Fuel Pins, Nucl. Technol. 70 (1985) 215–219. https://doi.org/10.13182/NT85-A33645.

[7] Y. de Carlan, J.-L. Bechade, P. Dubuisson, J.-L. Seran, P. Billot, A. Bougault, T. Cozzika, S. Doriot, D. Hamon, J. Henry, M. Ratti, N. Lochet, D. Nunes, P. Olier, T. Leblond, M.H. Mathon, CEA developments of new ferritic ODS alloys for nuclear applications, J. Nucl. Mater. 386–388 (2009) 430–432. https://doi.org/10.1016/j.jnucmat.2008.12.156.

[8] S. Ukai, S. Mizuta, M. Fujiwara, T. Okuda, T. Kobayashi, Development of 9Cr-ODS Martensitic Steel Claddings for Fuel Pins by means of Ferrite to Austenite Phase Transformation, J. Nucl. Sci. Technol. 39 (2002) 778–788. https://doi.org/10.1080/18811248.2002.9715260.

[9] L. Toualbi, C. Cayron, P. Olier, J. Malaplate, M. Praud, M.-H. Mathon, D. Bossu, E. Rouesne, A. Montani, R. Logé, Y. de Carlan, Assessment of a new fabrication route for Fe–9Cr–1W ODS cladding tubes, J. Nucl. Mater. 428 (2012) 47–53. https://doi.org/10.1016/j.jnucmat.2011.12.013.

[10] E. Vakhitova, D. Sornin, F. Barcelo, M. François, Texture evolution in Oxide Dispersion Strengthened (ODS) steel tubes during pilgering process, J. Nucl. Mater. 494 (2017) 20–28. https://doi.org/10.1016/j.jnucmat.2017.07.002.

[11] M. Yamamoto, S. Ukai, S. Hayashi, T. Kaito, S. Ohtsuka, Formation of residual ferrite in 9Cr-ODS ferritic steels, Mater. Sci. Eng. A. 527 (2010) 4418–4423. https://doi.org/10.1016/j.msea.2010.03.079.

[12] M. Yamamoto, S. Ukai, S. Hayashi, T. Kaito, S. Ohtsuka, Reverse phase transformation from α to γ in 9Cr-ODS ferritic steels, J. Nucl. Mater. 417 (2011) 237–240. https://doi.org/10.1016/j.jnucmat.2010.12.250.

[13] T. Yamashiro, S. Ukai, N. Oono, S. Ohtsuka, T. Kaito, Microstructural stability of 11Cr ODS steel, J. Nucl. Mater. 472 (2016) 247–251. https://doi.org/10.1016/j.jnucmat.2016.01.002.

[14] S. Ukai, S. Ohtsuka, T. Kaito, H. Sakasegawa, N. Chikata, S. Hayashi, S. Ohnuki, High-temperature strength characterization of advanced 9Cr-ODS ferritic steels, Mater. Sci. Eng. A. 510–511 (2009) 115–120. https://doi.org/10.1016/j.msea.2008.04.126.

[15] T. Tanno, S. Ohtsuka, Y. Yano, T. Kaito, Y. Oba, M. Ohnuma, S. Koyama, K. Tanaka, Evaluation of mechanical properties and nano-meso structures of 9–11%Cr ODS steels, J. Nucl. Mater. 440 (2013) 568–574. https://doi.org/10.1016/j.jnucmat.2013.04.006.

[16] H. Schnablegger, Y. Singh, The SAXS Guide, 3rd ed., n.d.

[17] B.L. Henke, E.M. Gullikson, J.C. Davis, X-Ray Interactions: Photoabsorption, Scattering, Transmission and Reflection, At. Data Nucl. Data Tables. 54 (1993). https://escholarship.org/uc/item/9wh2w9rg.

[18] B.R. Pauw, J.S. Pedersen, S. Tardif, M. Takata, B.B. Iversen, Improvements and considerations for size distribution retrieval from small-angle scattering data by Monte Carlo methods, J. Appl. Crystallogr. 46 (2013) 365–371. https://doi.org/10.1107/S0021889813001295.

[19] I. Bressler, B.R. Pauw, A.F. Thünemann, McSAS: software for the retrieval of model parameter distributions from scattering patterns, J. Appl. Crystallogr. 48 (2015) 962–969. https://doi.org/10.1107/S1600576715007347.

[20] S. Ukai, T. Kaito, S. Ohtsuka, T. Narita, M. Fujiwara, T. Kobayashi, Production and properties of nano-scale oxide dispersion strengthened (ODS) 9Cr martensitic steel claddings, ISIJ Int. 43 (2003) 2038–2045.

[21] C. Cayron, E. Rath, I. Chu, S. Launois, Microstructural evolution of Y2O3 and MgAl2O4 ODS EUROFER steels during their elaboration by mechanical milling and hot isostatic pressing, J. Nucl. Mater. 335 (2004) 83–102. https://doi.org/10.1016/j.jnucmat.2004.06.010.

[22] C. García de Andrés, Application of dilatometric analysis to the study of solid–solid phase transformations in steels, Mater. Charact. 48 (2002) 101–111. https://doi.org/10.1016/S1044-5803(02)00259-0.

[23] B. Hary, T. Guilbert, P. Wident, T. Baudin, R. Logé, Y. de Carlan, Investigation of the relationships between mechanical properties and microstructure in a Fe-9%Cr ODS steel, EPJ Nucl. Sci. Technol. 2 (2016) 7. https://doi.org/10.1051/epjn/e2016-50008-7.

[24] F. Abe, ed., Creep-resistant steels, CRC Press, Boca Raton, Fla., 2008.

[25] D.L. Sornin, A. Karch, R.E. Logé, Competition between intragranular and intergranular deformation mechanisms in ODS ferritic steels during hot deformation at high strain rate, J. Mater. Sci. 53 (2018) 2965–2975. https://doi.org/10.1007/s10853-017-1730-1.

[26] S.M.S. Aghamiri, T. Sowa, S. Ukai, N. Oono, K. Sakamoto, S. Yamashita, Microstructure and texture evolution and ring-tensile properties of recrystallized FeCrAl ODS cladding tubes, Mater. Sci. Eng. A. 771 (2020) 138636. https://doi.org/10.1016/j.msea.2019.138636.

[27] S. Atamert, J.E. King, Elemental partitioning and microstructural development in duplex stainless steel weld metal, Acta Metall. Mater. 39 (1991) 273–285. https://doi.org/10.1016/0956-7151(91)90306-L.

[28] S. Ohtsuka, T. Kaito, T. Tanno, Y. Yano, S. Koyama, K. Tanaka, Microstructure and high-temperature strength of high Cr ODS tempered martensitic steels, J. Nucl. Mater. 442 (2013) S89–S94. https://doi.org/10.1016/j.jnucmat.2013.06.010.

[29] A. Kumar, A. Dutta, S.K. Makineni, M. Herbig, R.H. Petrov, J. Sietsma, In-situ observation of strain partitioning and damage development in continuously cooled carbide-free bainitic steels using micro digital image correlation, Mater. Sci. Eng. A. 757 (2019) 107–116. https://doi.org/10.1016/j.msea.2019.04.098.

[30] M. Nowell, S. Wright, J. Carpenter, Differentiating Ferrite and Martensite in Steel Microstructures Using Electron Backscatter Diffraction, Aterials Sci. Technol. Conf. Exhib. 2009 MS T09. 2 (2009) 12.

[31] L. Mujica, S. Weber, H. Pinto, C. Thomy, F. Vollertsen, Microstructure and mechanical properties of laser-welded joints of TWIP and TRIP steels, Mater. Sci. Eng. A. 527 (2010) 2071–2078. https://doi.org/10.1016/j.msea.2009.11.050.

[32] T. Muroga, T. Nagasaka, Y. Li, H. Abe, S. Ukai, A. Kimura, T. Okuda, Fabrication and characterization of reference 9Cr and 12Cr-ODS low activation ferritic/martensitic steels, Fusion Eng. Des. 89 (2014) 1717–1722. https://doi.org/10.1016/j.fusengdes.2014.01.010.

[33] H.J. Frost, M.F. Ashby, Deformation-mechanism maps: the plasticity and creep of metals and ceramics, 1st ed, Pergamon Press, Oxford [Oxfordshire] ; New York, 1982.

[34] R.L. Klueh, J.P. Shingledecker, R.W. Swindeman, D.T. Hoelzer, Oxide dispersion-strengthened steels: A comparison of some commercial and experimental alloys, J. Nucl. Mater. 341 (2005) 103–114. https://doi.org/10.1016/j.jnucmat.2005.01.017.

[35] T. Kaito, S. Ohtsuka, M. Inoue, T. Asayama, T. Uwaba, S. Mizuta, S. Ukai, T. Furukawa, C. Ito, E. Kagota, R. Kitamura, T. Aoyama, T. Inoue, In-pile creep rupture properties of ODS ferritic steel claddings, J. Nucl. Mater. 386–388 (2009) 294–298. https://doi.org/10.1016/j.jnucmat.2008.12.117.

[36] H. Sakasegawa, S. Ukai, M. Tamura, S. Ohtsuka, H. Tanigawa, H. Ogiwara, A. Kohyama, M. Fujiwara, Creep constitutive equation of dual phase 9Cr-ODS steel, J. Nucl. Mater. 373 (2008) 82–89. https://doi.org/10.1016/j.jnucmat.2007.05.031.

[37] S.Y. Zhong, J. Ribis, V. Klosek, Y. de Carlan, N. Lochet, V. Ji, M.H. Mathon, Study of the thermal stability of nanoparticle distributions in an oxide dispersion strengthened (ODS) ferritic alloys, J. Nucl. Mater. 428 (2012) 154–159. https://doi.org/10.1016/j.jnucmat.2011.12.028.